LIP-STUDENTS-25-15

X-ray attenuation technique for target characterization: development and GUI implementation

Aysu Ismayilova[1,a] and Filipa Quadrilheiro[2,b]

[1] *Kaunas University of Technology, Kaunas, Lithuania*
[2] *Instituto Superior Técnico, Lisbon, Portugal*

Project supervisors: A. Vicente, M. Paulino, P. Teubig, R. Pires and T. Campante *September 30, 2025*

Abstract. Target fabrication plays an important role in nuclear astrophysics experiments. In the Target Design Laboratory at LIP/FCUL, various types of targets are produced, necessitating accurate characterization for their effective use. This report focuses on evaluating the X-Ray Attenuation (XRA) technique for characterizing both single and multilayered targets. The performance of XRA was assessed by comparing its results with those from established techniques such as Alpha Energy Loss (AEL) and Rutherford Backscattering Spectrometry (RBS). The findings not only contribute with valuable data to the process of benchmarking this technique, but also help determine its practical limitations. Furthermore, to perform the analysis of XRA measurements, a dedicated Graphical User Interface (GUI) was developed to facilitate thickness calculations.

Keywords: Thin films, Multilayered Targets, Rutherford Backscattering Spectrometry (RBS), Alpha energy loss (AEL), Graphical User Interface (GUI)

1 Introduction

1.1 Motivation

Thin film targets play a crucial role in experimental nuclear physics, serving as the interaction medium where nuclear reactions occur under controlled conditions. Their applications extend from fundamental studies of nuclear structures to practical uses in nuclear medicine and energy research. For such experiments, it is essential that the targets are mostly isotopically pure, chemically uniform, and precisely controlled in thickness, often ranging from nanometers to micrometers (Figure 1). To achieve these requirements, a wide range of fabrication methods is available, including physical vapor deposition, molecular plating [1], cold rolling, and solvent casting [2], each tailored to meet specific experimental needs [3].

However, the effectiveness of these targets depends not only on their fabrication, but also on their accurate characterization. Since nuclear reaction measurements are highly sensitive to factors such as thickness, uniformity, and composition, it is necessary to verify these properties with precision. Inadequate characterization may lead to significant uncertainties in target properties, which can affect the reliability of experimental results. Therefore, careful characterization represents an indispensable step in ensuring the accuracy of nuclear physics research.

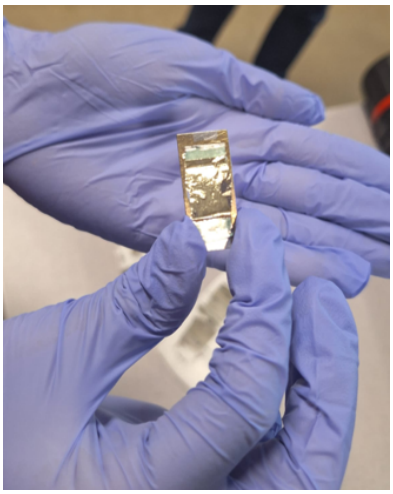

Figure 1: Thin film.

1.2 Target characterization

Several methods exist to characterize targets, such as Alpha Energy Loss (AEL), Rutherford Backscattering Spectrometry (RBS), and X-Ray Attenuation (XRA).

The reason why multiple methods are used to characterize thin films is that each technique provides information about specific properties. For example, the AEL technique can determine film thickness and uniformity, while the RBS technique is useful for detecting impurities in addition to thickness and uniformity. However, each method also has disadvantages: AEL may risk damaging the films due to the vacuum conditions, while RBS requires both a vacuum environment and significant beam time. In contrast, the XRA technique mainly provides thickness characterization, but it is a relatively simple method that does not require a vacuum environment.

1.2.1 Alpha Energy Loss

In the AEL technique, the thickness of a thin film is estimated by analyzing the energy loss of the alpha particles as they pass through the material. The material is placed between a radioactive source and a detector,

[a] e-mail: aysu.ismayilova@ktu.edu
[b] e-mail: filipa.quadrilheiro@tecnico.ulisboa.pt

and the difference between the transmitted energy and the reference vacuum energy reflects the energy lost in the film.

Under the Continuous Slowing Down Approximation (CSDA), the film thickness can be approximated, as in equation 1, by summing the energy loss over discrete steps using the tabulated stopping powers [4, 5].

$$\Delta x \approx \sum_{E_k=E_i}^{E_f} \frac{\delta E}{S(E_k)} \tag{1}$$

$S(E_k)$ corresponds to the stopping power at energy E_k, and $\delta E = E_{k+1} - E_k$. Figure 2 shows the experimental apparatus for AEL measurements at the Faculty of Sciences of the University of Lisbon [6].

Figure 2: AEL setup. Legend: 1 – Sample holder for the source; 2 – Thin film; 3 – Silicon Surface Barrier Detector (SSBD); 4 – Vacuum chamber.

In this setup, radioactive sources such as ^{232}U and ^{226}Ra are placed in the sample holder at the bottom. An SSB detector is mounted on top of the holder to measure the energy spectrum of emitted alpha particles. At the beginning of the experiment, a reference spectrum without any film is obtained, which represents the original alpha energies. For film spectrum measurements, a thin film is positioned on top of the radioactive source so that when the holder is mounted, the film lies between the source and the detector. In this configuration, the detector still records the transmitted alpha spectrum, but with the energy distribution modified by the presence of the film. By comparing the two spectra and applying Equation 1, the thickness of the film can be determined [7].

In the above-mentioned setup, additional apparatus includes a vacuum pump, high-voltage power supply, amplifier, oscilloscope, and a multichannel analyzer (Figure 3). The vacuum pump provides a controlled low-pressure environment, allowing alpha particles to travel from the source to the detector without significant energy loss due to air collisions. Meanwhile, a multichannel analyzer records the energies of the detected alpha particles and displays their energy spectrum.

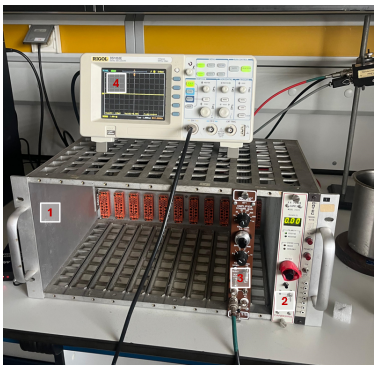

Figure 3: Electronics block. Legend: 1 – Nuclear Instrumentation Module (NIM) basket; 2 – High-voltage power supply; 3 – Amplifier; 4 – Oscilloscope.

An example of the data acquisition system display is shown in Figure 4. In this experiment, a ^{226}Ra source and a gold film were used to obtain the comparative energy spectra. The characteristic α energies for the Radium-226 decay are 7.69 MeV, 6.00 MeV, 5.49 MeV, 5.30 MeV, 4.78 MeV, 4.60 MeV [8].

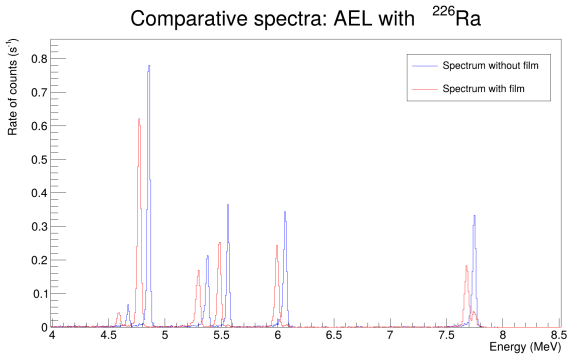

Figure 4: Comparative Spectra for AEL technique for a gold target.

1.2.2 Rutherford Backscattering Spectrometry

Another technique for target characterization is RBS. This technique is performed using the Van de Graaff accelerator shown in Figure 5 at CTN-IST (Centro Tecnológico Nuclear - Instituto Superior Técnico). This technique allows to obtain detailed information about the targets, such as their composition, thicknesses of different layers and the presence of impurities.

The 2.5 MeV Van de Graaff accelerator produces a proton or α beam, with energy up to 2.5 MeV, that irradiates the target sample. Most incident particles pass directly through the target. However, a small fraction is backscattered from the sample, and of these, only a few reach the detector. By placing a target in the RBS chamber, shown in Figure 6, that is hit by the accelerated beam, particles hitting the target will be backscattered, and can be detected by one of the detectors placed in the chamber, as illustrated in Figure 7.

Figure 5: Van de Graaff accelerator.

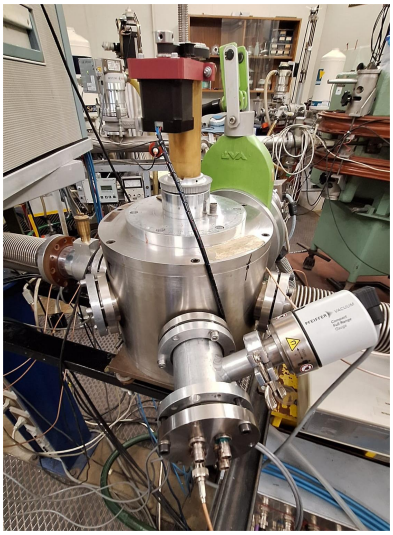

Figure 6: Vacuum chamber where the targets are placed.

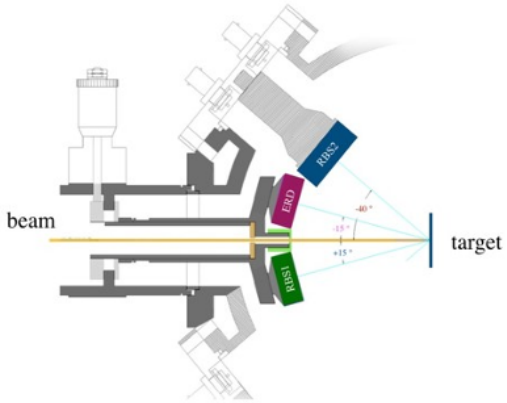

Figure 7: RBS chamber schematics. Three detectors, labeled RBS1, ERD, and RBS2, are found inside. The first two are placed at ±165° relative to the incident particle beam, and the third is at 140° [7].

Once the particles in the accelerated beam with an energy E_0 hit the target, some will interact with the atoms in the surface of the target and are backscattered right away. This beam of backscattered particles will have an energy E_{bs}. The ratio of the projectile energy after the collision to that before the collision can be defined as the kinematic factor, K, expressed in Equation 2:

$$K \equiv \frac{E_{bs}}{E_0} \tag{2}$$

The Kinematic Factor is given by Equation 3, knowing the mass of the projectile, M_1, the mass of an atom in the target examined, M_2, and the backscattering angle, θ [9].

$$K_{M_2} = \left[\frac{\left(1 - \left(\frac{M_1}{M_2}\right)^2 \sin^2\theta\right)^{\frac{1}{2}} + \frac{M_1}{M_2}\cos\theta}{1 + \frac{M_1}{M_2}} \right]^2 \tag{3}$$

Other particles will penetrate the surface of the target, losing energy as they do so, and be backscattered when interacting with an atom deeper in the target. Therefore, they will reach the detector with lower energies the deeper they penetrate the target before being backscattered. Given the energies where the peak starts and ends, it is possible to determine the thickness and element of that target layer.

The thickness is given by Equation 4 where ΔE is the energy interval of the peak and $[S]$ is the Energy Loss Factor. $[S]$ can be determined with Equation 5 where θ_1 is the angle that the normal of the target makes with the normal of the incident particle beam and θ_2 is the angle that the backscattered particle beam makes with the incident particle beam. The $(dE/dx)_{in}$ is the stopping power for the energy of the incident beam and $(dE/dx)_{out}$ is the stopping power for the energy of the beam after being backscattered; since a proton beam was used, these values can be found in the NIST PSTAR database [10].

$$x = \frac{\Delta E}{[S]} \tag{4}$$

$$[S] \equiv \left[\frac{K}{\cos\theta_1} \left.\frac{dE}{dx}\right|_{in} + \frac{1}{\cos\theta_2} \left.\frac{dE}{dx}\right|_{out} \right] \tag{5}$$

The measurements are confirmed with simulations using SIMNRA [11]. In these simulations, by adjusting parameters such as the thickness of the target, we look for a simulated curve that better fits the experimental data. This way, it is possible to characterize the targets.

1.2.3 X-Ray Attenuation (XRA)

Now we will take a look at the method of target characterization, which was the main focus during this internship, the X-ray attenuation method. Starting by briefly explaining how the X-rays are produced and then explaining how their interaction with matter can allow us to determine the thickness of targets.

X-Ray production

Once an atom from a given element is hit by an ionizing particle, one of its electrons from one of the inner electronic shells can be ejected if the incident particle transfers at least the binding energy of that electron. When this happens, the atom will be left with an "empty spot" in one of its electronic shells. This spot will be filled with a captured electron from the medium or an electron from an outer shell of the atom, as illustrated in Figure 8. This electronic rearrangement of the atom (de-excitation) will release a photon with an energy equal to the energetic difference of the two shells involved in the transition - a phenomenon called X-ray fluorescence. In some cases, instead of X-ray emission, an outer shell electron may be ejected as a relaxation route (known as Auger effect).

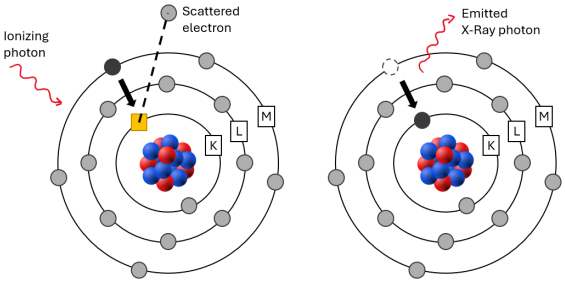

Figure 8: Schematics of X-ray production by high-energy photon excitation. Adapted from [12].

Each element has different binding energies for electrons from different electronic shells, thus each element will emit X-rays with different characteristic energies. The X-rays are classified with the Siegbahn notation, depending on the initial and final electronic shells of the transition. Given the designations for the shells shown in the schematics, for example, when an empty spot is created in the K shell and it is filled with an electron from the L shell, the X-rays are classified as K-α; if it is filled with an electron from the M shell the X-rays are classified as K-β, which have a higher energy. If, instead, an empty spot is filled with a free electron from the medium, the maximum X-ray energy of the K series would be obtained. The same logic applies to different transitions between different atomic shells originating to L and M series [13].

The Method

When an X-ray beam crosses a material, its intensity is reduced by a process known as attenuation. This attenuation results from photon interactions with matter, primarily through the photoelectric effect and Compton interaction [13]. These processes effectively remove photons from the incident beam, leading to an emergent beam with lower intensity, as illustrated in Figure 9.

The empirical Beer-Lambert's law, shown in Equation 6, relates the intensity of the attenuated X-ray beam, I, after crossing a layer of material with the intensity of the incident X-ray beam, I_0. The attenuation depends on two things: the thickness of the target, x, and the attenuation coefficient, μ, which depends on the element present in our substrate of matter and the energy of the X-rays.

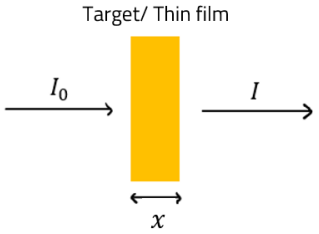

Figure 9: X-Ray attenuation schematics.

$$I = I_0 e^{-\mu x} \tag{6}$$

$$x = \frac{1}{\mu} \ln\left(\frac{I_0}{I}\right) \tag{7}$$

The aim is to know the thickness of a target. Therefore, knowing the intensities of the X-ray beams before and after being attenuated and the attenuation coefficient, it is possible to determine the thickness using Equation 7. The mass attenuation coefficient values, $[\mu/\rho]$, used for calculations were taken from the NIST XCOM database [14]. For that, a setup is necessary that allows to obtain the spectrum of the incident X-ray beam, I_0, by measuring the X-ray beam from the source and the spectrum of the attenuated X-ray beam, I, by measuring the spectrum with the target in front of the source. The obtained spectra are translated into the rate of counts per energy, where the intensity will be the rate of counts under the characteristic X-ray lines of the element used to produce the X-rays. As an example, for the measurements made with a copper X-ray source, it is possible to observe the comparison of both spectra shown in Figure 10, where the attenuated spectrum falls shorter in the rate of counts compared to the incident beam spectrum.

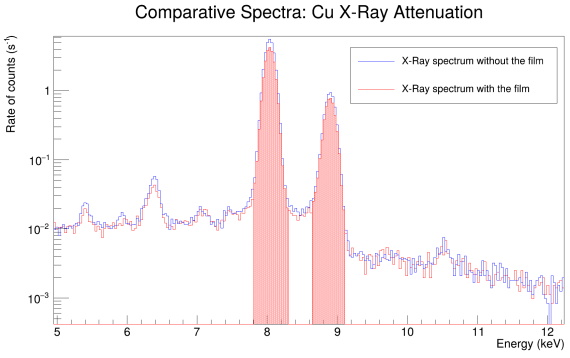

Figure 10: Comparative spectra from an example of a measurement using the X-ray attenuation technique. The colored area under the copper peaks represents the integrated area to obtain the intensities.

A factor that needs to be considered with this technique is the contribution of background radiation to the measurements. The background radiation should be measured for a sufficiently long period of time to obtain reliable statistics, as the rate of counts for the background radiation is very low. Taking this into consideration, the thickness will be calculated using Equation 8:

$$x = \frac{1}{\mu} \ln\left(\frac{I_0 - I_{bkg}}{I - I_{bkg}}\right) = \frac{1}{\mu} \ln\left(\frac{I'_0}{I'}\right) \tag{8}$$

Where I_{bkg} denotes the background radiation intensity, and $I'_0 = I_0 - I_{bkg}$ and $I' = I - I_{bkg}$ are the corrected intensities. The uncertainty for x is given by Equation 9, in which t, t_0 and t_{bkg} represent the acquisition time for their respective measured intensity.

$$\sigma_x = \sqrt{\frac{I_0}{t_0\, I'^2_0} + \frac{I}{t\, I'^2} + \frac{I_{bkg}\,(I_0 - I)^2}{t_{bkg}\, I'^2_0\, I'^2}} \tag{9}$$

This method has some advantages when compared to the two previously discussed. It does not require vacuum because the attenuation of the X-rays in the air can be disregarded. This happens for two reasons: i) the beam attenuation in air is far less intense compared to the attenuation occurring in the target, so the count rate is not considerably affected by air, especially, considering the detector is at a very short distance from the source; ii) the distance from the detector to the source is the same in the measurements to obtain I and I_0, and we are going to use the ratio I'_0/I' in our calculations so the contribution of the air attenuation cancels out. This reduces the probability of damaging targets compared to a vacuum environment situation. Additionally, this method can be done with a simple setup and does not require visits to external laboratories, as it is the case with the RBS technique. Lastly, and most importantly for this internship, this method can potentially allows determining the thickness of a film layer even through a coating of another material, as long as the coating is not very thick and the attenuation coefficients are substantially different, which happens for materials with very different atomic numbers - the higher the atomic number, the greater the attenuation. This aspect of the technique will be looked further into in section 4.

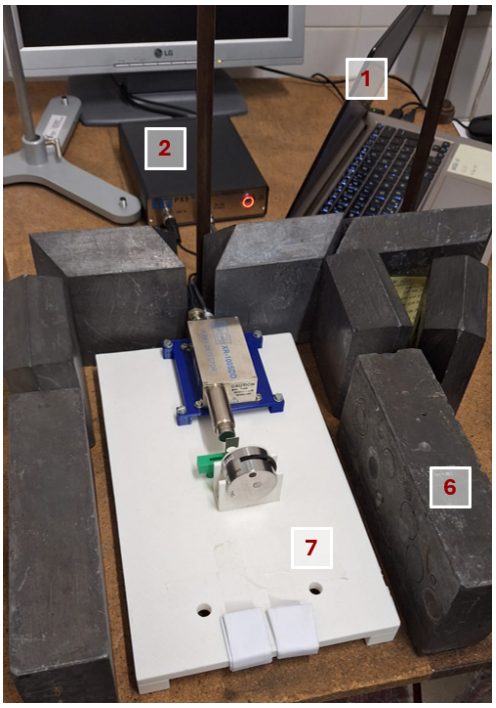

(a) General view

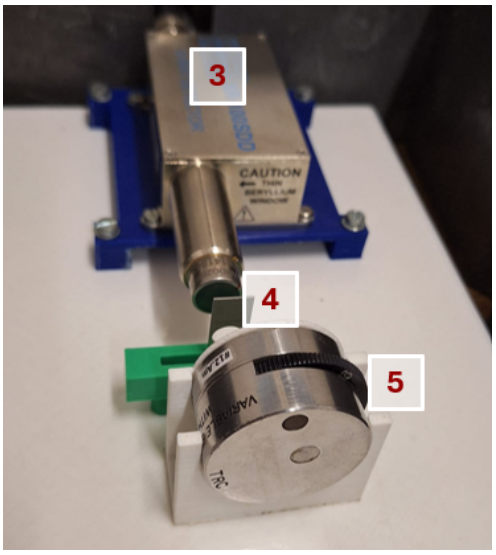

(b) Detailed view

Figure 11: Experimental setup for XRA measurements. Legend: 1 – Computer with DPPMCA Display and Acquisition Software; 2 – Digital pulse processor; 3 – Silicon detector; 4 – Thin film; 5 – X-ray source; 6 – Lead bricks; 7 – Detector and source support.

2 XRA experimental setup and detector

Given the method explained in the previous section, the experimental setup presented in Figure 11 was used to conduct the measurements. It consists of a variable X-ray source, a silicon detector, a digital pulse processor, a computer with an acquisition and display software capable of recording the energy spectrum of the source, and an acquisition station that fixes the positions of the source, the detector and the target.

The variable X-ray source uses a ^{241}Am radioactive source, and a rotating wheel with six different materials, as seen in Figure 12. Americium-241 decays (by alpha decay) to Neptunium-237, a gamma emitter whose photons will interact with the selected material from the wheel, as previously explained, to produce X-rays. The materials in this source are copper, rubidium, molybdenum, silver, barium and terbium, each with its characteristic X-ray energies.

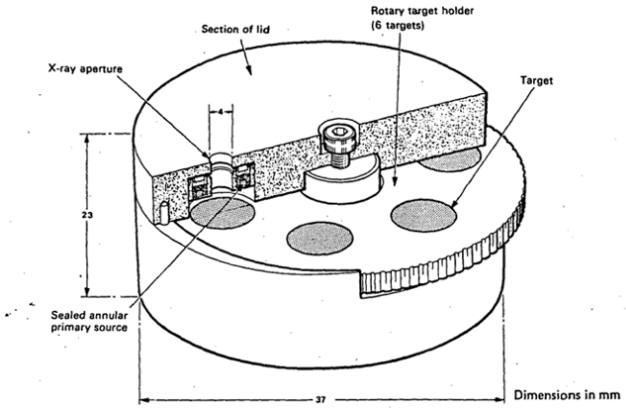

Figure 12: X-ray source with a rotating wheel with 6 elements Cu, Rb, Mo, Ag, Ba, Tb. Taken from [15].

In this setup, an AmpTek XR-100SDD Silicon Drift Detector (SDD) [16] was used, for which the schematics are recreated in Figure 13. The detector is composed of a beryllium window that the X-ray beam crosses as it reaches the detector, surrounded by a nickel cover. The detector uses a four-layer collimator, which shortens the radius of the X-ray beam that reaches the silicon crystal.

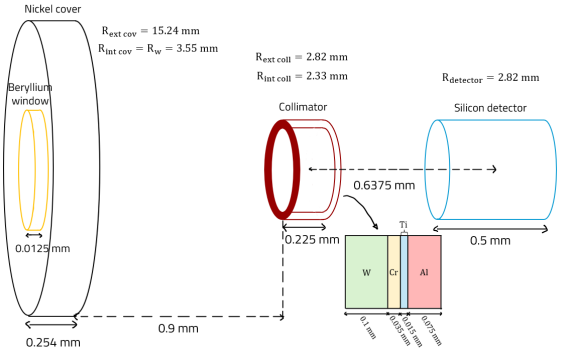

Figure 13: Schematics of the X-ray detector

2.1 Study of the X-ray detector

2.1.1 Chanel-Energy calibration

The detection system utilizes a silicon detector, which generates an analog signal proportional to the energy of an incident particle. The MCA digitizes the amplitude of the signal by subdividing its range into 2048 channels. The relationship between the particle energy and the corresponding channel number is a characteristic of the system that can be determined experimentally.

A linear relationship between channel number and energy is assumed, defined by the Equation 10:

$$E = k \cdot Ch + b \tag{10}$$

Where E is energy, Ch is the channel number, k is the energy per channel, and b is an offset. To perform the calibration, spectra are acquired from the six known elements in the X-ray source. The characteristic X-ray line values were taken from [17]. The linear regression is performed as shown in Figure 14. The parameters obtained from the fit were:

$$k = (31.08 \pm 0.02)\,\text{eV Ch}^{-1}$$
$$b = (-30 \pm 10)\,\text{eV}$$

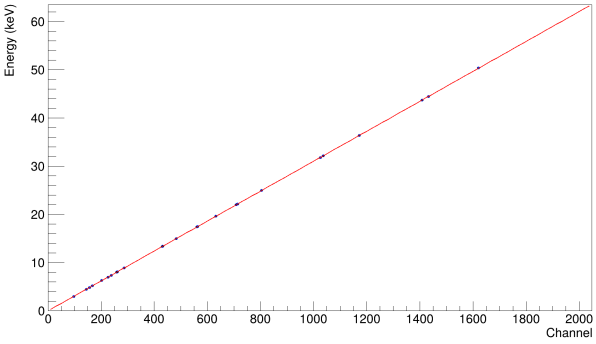

Figure 14: Energy-channel calibration. The channel number of characteristic X-ray peaks is plotted as a function of their known energy.

2.1.2 Resolution-Energy calibration

The energy resolution of a detector quantifies its ability to distinguish between particles with similar energies. Although X-rays are emitted at discrete energies, due to the imperfect resolution of the detection system the X-ray spectrum exhibits a distribution of counts over a range of channels rather than a single channel. This is due to the statistical fluctuations and electronic noise inherent to the detection process. For this work, Gaussian fits were used for the peaks. The centroid of the Gaussian fit done to a peak corresponds to the most probable energy value, while its width characterizes the detector's resolution.

The energy resolution, R, is conventionally defined as the Full Width at Half Maximum (FWHM) of a peak divided by its centroid energy, E [18]. For a Gaussian distribution, the FWHM is related to the standard deviation, σ_E, obtained from the fit. Thus, the resolution is calculated as:

$$R = \frac{\text{FWHM}}{E} = \frac{2\sqrt{2\ln 2}\cdot\sigma_E}{E} \tag{11}$$

To define how the resolution depends on energy, the same set of spectra used for the energy-channel calibration was analyzed, and the characteristic X-ray peaks from the six known elements (Cu, Mo, Zr, Ag, Ba, and Tb) were fitted with Gaussian functions on the energy-calibrated spectrum. From each fit, the centroid energy, E, and its standard deviation σ_E were extracted. The resolution, R, was then calculated for each peak using Equation 11.

The dependence of resolution on energy is modeled by:

$$R = k \cdot \frac{1}{\sqrt{E}} + b \tag{12}$$

A linear regression was performed on this data, as shown in Figure 15, to determine the constants k and b that best describe the detector's performance across the measured energy range. The parameters obtained from the fit were:

$$k = (1.9 \pm 0.5)\,\mathrm{keV}^{\frac{1}{2}}$$
$$b = (-1 \pm 3) \times 10^{-3}$$

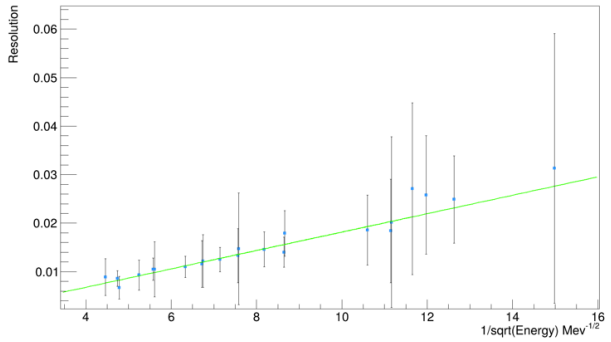

Figure 15: Energy resolution calibration. The resolution R is plotted as a function of $1/\sqrt{E}$.

2.1.3 Efficiency

An important characteristic of a detector is its efficiency, which was studied using TOPAS simulations. TOPAS is a Monte Carlo simulation tool based on Geant4, used to model particle interactions with matter [19]. The experimental setup was simulated, including the detector as shown in Figure 13.

The total detection efficiency, ϵ, is the product of the intrinsic and geometrical efficiencies:

$$\epsilon = \epsilon_i \cdot \epsilon_g \tag{13}$$

Intrinsic Efficiency

The intrinsic efficiency, ϵ_i, is an energy-dependent property of the detector, representing its probability of detecting a particle that reaches its active volume. It is defined as:

$$\epsilon_i = \frac{N_{\text{detected}}}{N_{\text{incident}}} \tag{14}$$

where N_{detected} is the number of events recorded and N_{incident} is the total number of particles reaching the detector.

To determine the intrinsic efficiency curve, TOPAS simulations were performed using a photon beam with a known energy incident directly on the detector face, across a range of energies. To generate realistic spectra, the raw energy deposition data from TOPAS was processed by applying Gaussian energy broadening based on the detector's resolution. This transformed the idealized energy deposit into Gaussian peaks that better represent what is observed in experimental measurements. The number of detected counts, N_{detected}, for each energy was obtained by integrating the counts under the corresponding Gaussian X-Ray peak within an interval of $\pm 3\sigma$ around its centroid. The resulting intrinsic efficiency values are plotted in blue in Figure 16.

Geometrical Efficiency

The geometrical efficiency, ϵ_g, is determined only by the detector's geometry and its position relative to the source. It represents the fraction of particles emitted from the source (considering an isotropic source) that intersect the detector's active area. The theoretical geometrical efficiency is given by Equation 15.

$$\epsilon_g = \frac{\Omega}{4\pi} \tag{15}$$

Where 4π is the total solid angle for an isotropic emission and Ω is the solid angle of the detector in relation to the source. For small aperture detectors, their solid angle can be calculated through the approximation in Equation 16, where d refers to the distance of the source to the collimator and r is the internal radius of the collimator (radius of the X-ray beam that reaches the target).

$$\Omega = 2\pi\left(1 - \frac{d}{\sqrt{d^2 + r^2}}\right) \tag{16}$$

Based on the geometry of the experimental setup, the theoretical geometrical efficiency calculated was 0.15 %. This result is shown as the red line in the plot in Figure 16.

Total Efficiency

The total efficiency curve shown in Figure 17 was computed by multiplying the intrinsic efficiency from the data points from the simulations by the value of the geometrical efficiency. The efficiency curve obtained from the simulated data is very similar to the one shown in the AMP-TEK manuals for this detector that can be consulted in [16], which confirms the validity of the obtained curve.

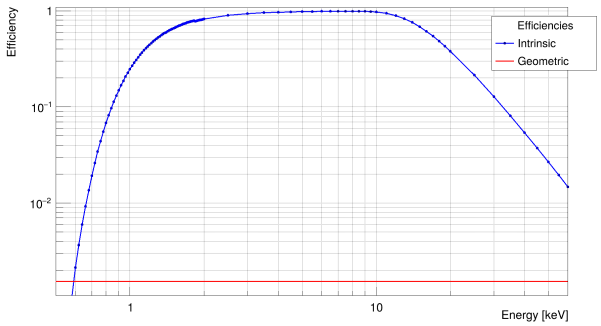

Figure 16: Detector efficiencies. The blue curve shows the intrinsic efficiency. The red line shows the theoretical value for the geometrical efficiency.

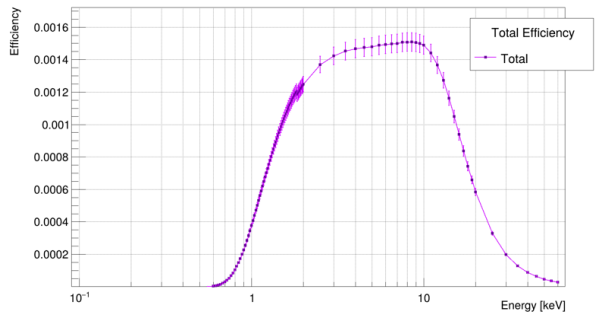

Figure 17: Total detection efficiency as a function of energy, obtained from the product of the simulated intrinsic and geometrical efficiencies.

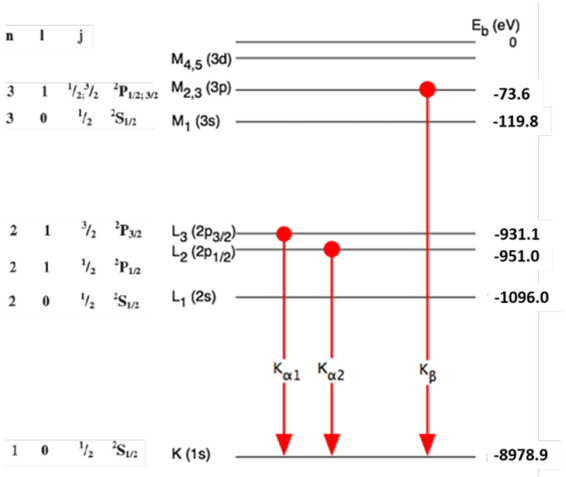

Figure 18: Schematics showing the copper X-ray energies [9].

For the measurements done with the XRA technique, a copper X-ray source was selected because the characteristic copper emissions at 8.048 keV (K_{α_1}), 8.02 keV (K_{α_2}), and 8.905 keV (K_{β_1}) as shown in the schematics in Figure 18 fall within the energy range of the detector's highest efficiency.

3 Graphical Interface

During the 2023 LIP summer internship, a Graphical User Interface (GUI) named ARC-TF was developed to enable users to calculate film thickness using the AEL technique [20]. To further support the determination of film thickness from X-ray attenuation measurements, the dedicated GUI has been improved and documented on a GitHub repository [21]. The interface provides a user-friendly environment for analyzing experimental data efficiently and accurately.

3.1 Purpose of the interface

The main goal of the interface is to reduce the time required for thin film characterization and to allow users to calculate film thickness using the XRA method.

3.2 Features and improvements

The addition of XRA functionality to the interface allows users to characterize films without the need for a vacuum environment, increasing the convenience of the method.

The interface includes options for file upload, region of interest (ROI) selection, and automatic thickness calculation using either database values or user-provided attenuation coefficients. A new "XRA" button has been added to the tab selector menu (Figure 19), allowing users to access the X-ray attenuation analysis on the interface. Once the XRA tab is opened, the user can now upload data files from the experiments to plot the graph (Figure 20).

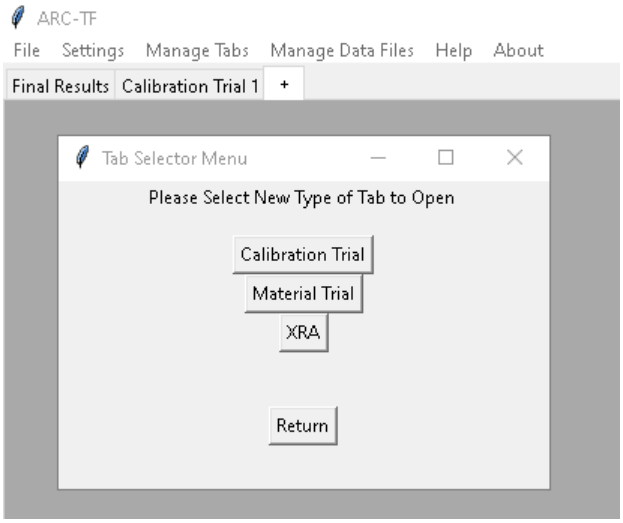

Figure 19: Tab selector menu.

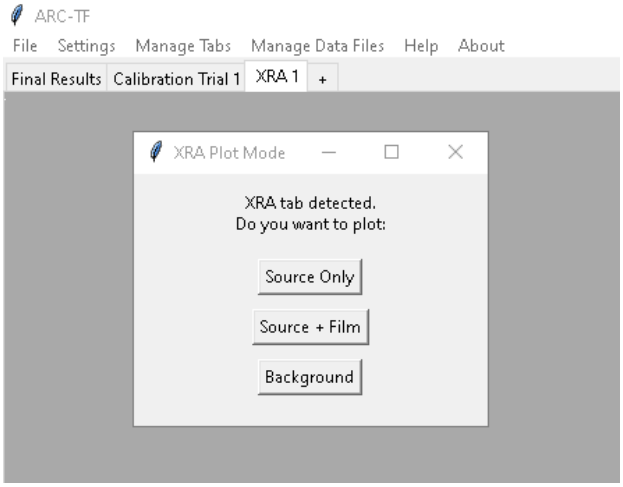

Figure 20: Plot data menu.

After uploading the necessary files, the interface is displayed as in Figure 21. At this stage, the user should define and input the ROI corresponding to the emission line region they wish to study. In Figure 21, a Sn film and a Cu X-ray source were used during the experiment. Once

ROI is selected, the interface applies a Gaussian fit, from which it extracts key parameters such as the centroid, the sigma, and the area under the curve for each case: source, film, and background (only area). Below this output, the user is prompted to select the preferred attenuation coefficient method for further analysis (Figure 22).

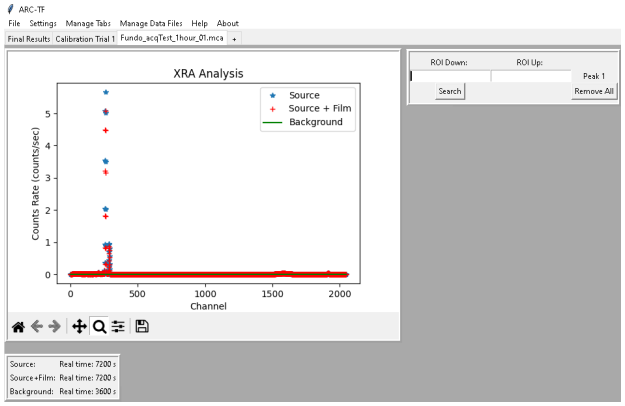

Figure 21: Interface view after files have been uploaded.

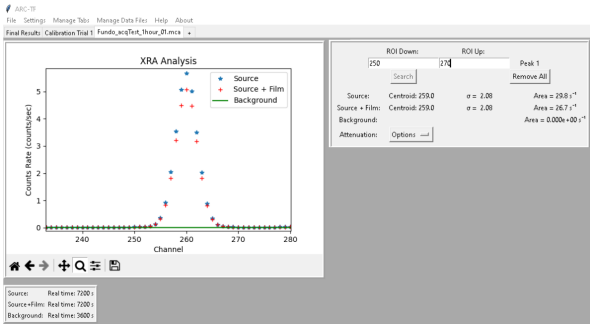

Figure 22: Interface view after ROI entry.

As shown in Figure 23, the user is provided with two options: either to use the default setting or to provide a custom input. If the default setting is chosen, the user can then specify the film material (Figure 24) and the X-ray source (Figure 25), and the corresponding attenuation coefficient is automatically retrieved from the database.

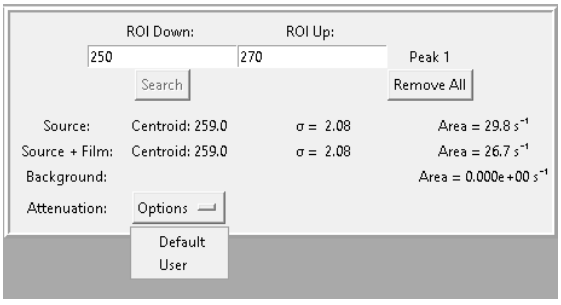

Figure 23: Attenuation coefficient selection options.

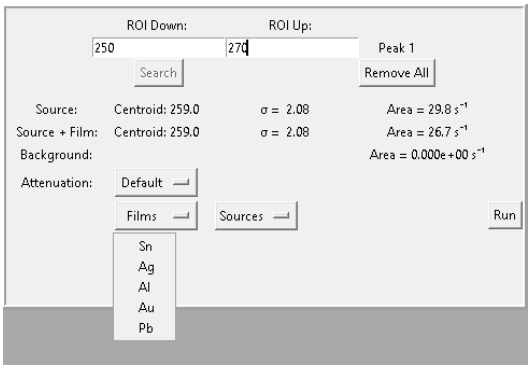

Figure 24: Default film material selection.

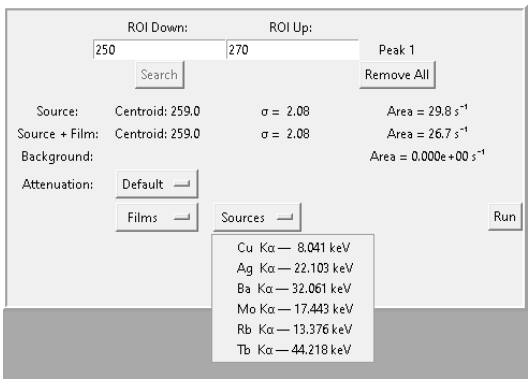

Figure 25: Default source selection.

Finally, when the "Run" button is clicked, the film thickness is calculated and displayed (Figure 26). As an alternative, the user input option is typically chosen when the film material or the source used in the experiment is not available in the database. In this case, the user can manually enter the linear attenuation coefficient to calculate the thickness of the film (Figure 27).

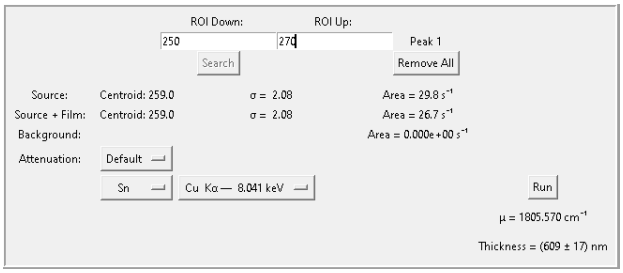

Figure 26: Thickness calculation.

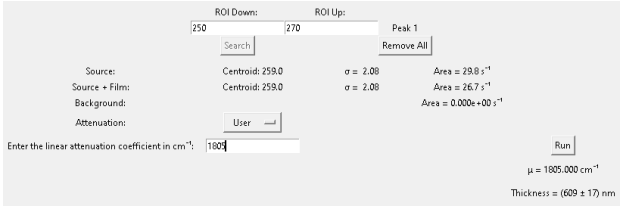

Figure 27: User input coefficient selection.

4 Results

4.1 One-layered films

As previously discussed in section 2.1.3, for the measurements, the characteristic copper X-rays were used, with Figure 28 depicting the obtained spectrum. The combined K_α peak (8.048 keV and 8.028 keV), which appears as a single peak due to the limited detector resolution, was used to obtain the intensities of the X-ray beams that allow for thickness calculations.

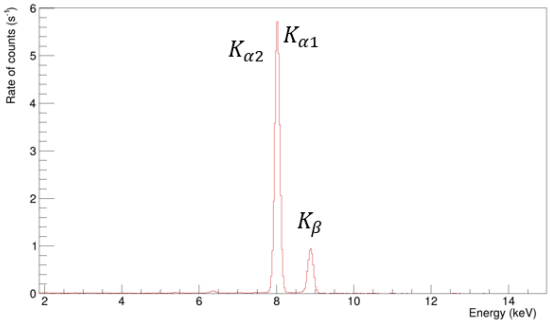

Figure 28: Copper X-ray energy spectrum

After the successful implementation of the XRA technique in the GUI, comparisons were made between its results and those obtained from the previously implemented AEL technique.

Table 1 presents the Au and Pb film thicknesses obtained with both techniques, as calculated in the interface. For the Au film thickness, when uncertainties are taken into account, the values are found to be comparable. Meanwhile, in the case of the Pb film, the results obtained by the two techniques are nearly identical.

Table 1: Single-layered film thicknesses evaluated by XRA and AEL, used to test the GUI developments.

Target	AEL [μm]	XRA [μm]
Au	0.19 ± 0.02	0.16 ± 0.01
Pb	1.96 ± 0.03	1.96 ± 0.02

As expected, the results confirm the capability of the XRA technique to characterize simple, one-layered films. The two measured targets demonstrate that this method can be applied to both relatively thick films (> 1 μm) and thin films (< 200 nm).

4.2 Multilayered films

As discussed in section 1.2.3, one advantage of the X-ray attenuation technique is its ability to characterize one of the layers in multilayered targets under appropriate conditions. To demonstrate this, measurements were performed on three different target types: tin and aluminum (Sn-Al), silver and aluminum (Ag-Al), and gold and aluminum (Au-Al). In each case, an aluminum coating overlayed a substrate of higher atomic number material. The difference in atomic number between aluminium (Z = 13) and the substrate materials (Sn: Z = 50, Ag: Z = 47, Au: Z = 79) results in substantially different attenuation coefficients, enabling the characterization of the layer even with an aluminum coating.

To benchmark the X-ray attenuation results, comparative measurements were done using alternative techniques. For the Sn-Al and Au-Al targets, previously obtained RBS and AEL results were used for comparison. For the Ag-Al target, new RBS measurements were performed using a 1.9 MeV proton beam. Three RBS measurements were taken at different locations on each target to increase statistics and to account for the non-uniformity of the sample. The thicknesses were calculated from the RBS spectra according to the methodology introduced in section 1.2.2, and the average of the three measurements was used for comparison. These experimental results were further validated by simulations performed with SIMNRA, as illustrated in Figure 29.

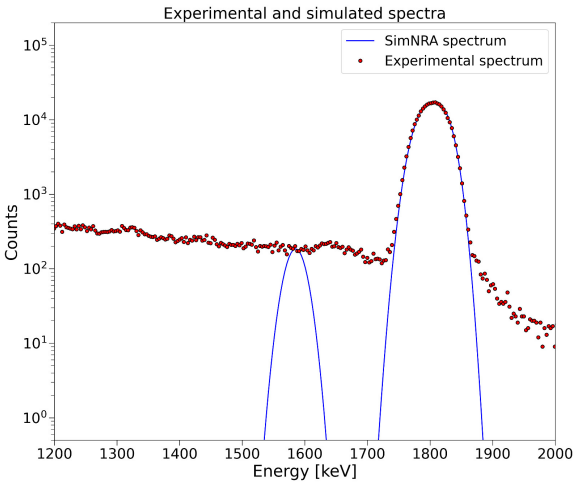

Figure 29: Experimental data for a silver target with aluminum coating and simulation of the aluminum (left) and silver (right) layers of the target and beam using SIMNRA.

As we can see, only one layer has a visible peak, which corresponds to the Ag layer; the Al layer was omitted by a plateau generated by protons backscattered in the vacuum chamber, after crossing the target. Although this prevents an accurate quantification of the thickness of the Al layer, it still allows the establishment of an upper limit of 60 nm for the thickness. Furthermore, as the XRA measurements were focused on the Ag layer, the RBS measurements are still useful for our discussion. A comparison between the calculated and simulated thicknesses is presented in Table 2. An agreement between the calculated values and the one obtained from the simulations can be observed with discrepancies bellow 3 %, which confirms the validity of the calculated values.

The final thickness values for the multilayered targets are shown in Table 3. For the RBS measurements, the

Table 2: Comparison of target thicknesses between theoretically calculated values and SIMNRA simulations, for the RBS technique.

Target	RBS (calc) [μm]	RBS (SIMNRA) [μm]	Error [%]
Au-Al-1	0.402 ± 0.016	0.410 ± 0.002	2.5
Au-Al-2	0.386 ± 0.016	0.396 ± 0.006	1.2
Au-Al-3	0.340 ± 0.016	0.336 ± 0.003	2.1

presented results are the average value from analytical calculations for each target. As for their uncertainties, they were defined according to the higher value obtained from two calculations: either the difference between the the thicknesses obtained from analytical calculations and SIMNRA simulations, or the maximum deviation of individual calculations from their average.

Table 3: Thickness comparison of multilayered targets from XRA measurements and other techniques. The other method used to calculate the thickness was RBS except for the target with * where the thickness was obtained only with AEL technique.

Target	XRA [μm]	Other Method [μm]	Error [%]
Sn-Al-1*	1.61 ± 0.10	1.59 ± 0.06	1.3
Sn-Al-2	1.23 ± 0.04	1.34 ± 0.08	8.1
Ag-Al-1	0.43 ± 0.01	0.40 ± 0.02	7.5
Ag-Al-2	0.41 ± 0.01	0.39 ± 0.02	5.1
Ag-Al-3	0.34 ± 0.01	0.35 ± 0.02	2.9
Au-Al-1	$(39 \pm 8) \times 10^{-3}$	$(11.2 \pm 0.2) \times 10^{-3}$	320
Au-Al-2	$(48 \pm 8) \times 10^{-3}$	$(12.4 \pm 0.2) \times 10^{-3}$	287
Au-Al-3	$(35 \pm 8) \times 10^{-3}$	$(12.6 \pm 0.3) \times 10^{-3}$	192

From the results of the measurements shown in the Table 3 we find two different outcomes. For the Sn-Al and the Ag-Al targets the results from the XRA technique are in close agreement with the results obtained through other technique. The same does not apply to the Au-Al targets, the results from the XRA technique are far different from the results from RBS.

5 Conclusions

The results presented in subsection 4.1 demonstrate that the XRA method implemented in the GUI successfully characterized the one-layered targets, yielding values that agree with those obtained using the AEL technique within the same interface. This validates both the capability of XRA for single-layered target characterization and the reliability of the implemented GUI.

For multilayered targets, the technique performed adequately in some cases. For the Sn-Al and Ag-Al targets, thicknesses determined via XRA showed good correspondence with the AEL and RBS reference techniques, with discrepancies generally remaining below 10 %. This confirms that XRA can provide reliable characterization for certain multilayer configurations. However, significant deviations were observed for the Au-Al targets, where the XRA results are considerably different from the RBS results. This discrepancy is due to the gold layer being too thin ($\approx$ 10 nm) compared to the aluminum ($\approx$ 700 nm to 800 nm). In these targets, the aluminum layer substantially attenuates the X-ray signal, compromising the reliability of the thickness determination. These results indicate that while XRA is a valuable characterization tool for multilayered targets, it has inherent limitations. To predict the applicability of this technique, analytical calculations or TOPAS simulations of the experimental setup could be performed. By simulating and obtaining the expected errors for the thicknesses across a range of thickness combinations, it would be possible to define boundaries for the reliability of the XRA characterization. Overall, the results obtained in this study provide valuable experimental data that contribute to improving the ongoing development of a benchmarking for the XRA technique. Additionally, the analysis and work done regarding the study of the X-ray detector help us get a better idea of the functioning of the experimental setup used for XRA measurements.

Acknowledgements

We would like to thank our supervisors Afonso Vicente, Margarida Paulino, Pamela Teubig, Ricardo Pires and Tomás Campante for their guidance and support through the course of our internships. We also want to thank the NUC-RIA group for welcoming us and to the LIP Internships program for the opportunity in taking part in this enriching experience.

References

[1] A. Muggleton, *Deposition techniques for the preparation of thin film nuclear targets*, Vacuum **37**, 785 (1987), https://doi.org/10.1016/0042-207X(87)90180-1

[2] A. Stolarz, *Target preparation for research with charged projectiles*, J Rad. Nuc. Chem. **299**, 913 (2014), https://doi.org/10.1007/s10967-013-2652-2

[3] N.E. Esker, A. Ard, et al., *Development of nuclear target production and characterization capabilities at san josé state university*, EPJ Web of Conferences **327**, 01015 (2025), https://doi.org/10.1051/epjconf/202532701015

[4] NIST, *ASTAR: Stopping Power and Range Tables for Helium Ions*, https://physics.nist.gov/PhysRefData/Star/Text/ASTAR.html, [Online; accessed 2025]

[5] NIST, *Appendix: Significance of Calculated Quantities*, https://physics.nist.gov/PhysRefData/Star/Text/appendix.html (2019), [Online; accessed 2025]

[6] L. Peralta, A.I. Campos, M.S. Rodrigues, *Thickness and uniformity of commercial aluminum foils*, Journal of Materials Engineering and Performance **34**, 9637 (2025), https://doi.org/10.1007/s11665-025-10722-8

[7] M. Paulino, R. Nunes, *Target preparation at FCUL* (2022), LIP-STUDENTS-22-22, https://www.lip.pt/files/training/papers/2022/pdf/LIP-STUDENTS-22-22-Nucria.pdf

[8] International Atomic Energy Agency (IAEA), *A-2. Alpha-particle energies and emission probabilities for actinides and natural decay products)*, https://www-nds.iaea.org/sgnucdat/a2.htm, [Online; accessed 2025]

[9] W.K. Chu, J.W. Mayer, M.A. Nicolet, *Backscattering Spectroscopy* (Academic press, 1978)

[10] NIST, *PSTAR: Stopping Power and Range Tables for Protons*, https://physics.nist.gov/PhysRefData/Star/Text/PSTAR.html, [Online; accessed 2025]

[11] M. Mayer, *SIMNRA: Simulation of RBS, ERD and NRA*, https://home.mpcdf.mpg.de/~mam/ (1997), [Software; current version consulted in 2025]

[12] Minepostol / FavPNG, *Atomic nucleus Bohr model — mass number / nucleon diagram*, https://favpng.com/png_view/nuclear-atomic-nucleus-bohr-model-mass-number-nucleon-png/M6Wkyf3c, [Online image; accessed 2025-09-27]

[13] V.A. Streltsov, C.T. Chantler, et al., *X-ray absorption*, Laboratory and Computational Physics **3** (2017)

[14] NIST, *XCOM: Photon Cross Sections Database*, https://physics.nist.gov/PhysRefData/Xcom/html/xcom1.html, [Online; accessed 2025]

[15] Department of the army, *Environmental Assessment and finding of no significant impact for the Am-241 variable energy X-ray Source*, https://www.nrc.gov/docs/ML0705/ML070590724.pdf (1985), [Online; accessed 2025]

[16] Amptek, *XR-100SDD Silicon Drift Detector*, https://www.amptek.com/internal-products/obsolete-products/sdd-x-ray-detectors-for-xrf/xr-100sdd-silicon-drift-detector, [Online; accessed 2025-09-26]

[17] Lawrence Berkeley National Laboratory (LBL), *X-Ray Data Booklet, Table 1-2: Energies of principal K, L, M shell emission lines*, https://xdb.lbl.gov/Section1/Table_1-2.pdf, [Online; accessed 2025-09-27]

[18] G.E. Knoll, *Radiation Detection and Measurement* (John Wiley Sons, Inc., 2000)

[19] TOPAS Collaboration, *TOol for PArticle Simulation (TOPAS)*, http://www.topasmc.org/ (2012), [Software; accessed 2025]

[20] A. Gusmão, *Developing a GUI for thin film characterization* (2023), LIP-STUDENTS-23-15, https://www.lip.pt/files/training/papers/2023/pdf/2023-PAPER-179-15.pdf

[21] A. Gusmão, et al., *ARC-TF*, https://github.com/RiPires/GUI_thin_films, [Online; accessed 2025]